Analytical Inversion Formula for Uniformly Attenuated Fan-Beam Projections

Yi Weng, Gengsheng L. Zeng, *Member, IEEE*, and Grant T. Gullberg, *Senior Member, IEEE*

***Abstract*— A convolution backprojection algorithm was derived by Tretiak and Metz to reconstruct two-dimensional (2-D) transaxial slices from uniformly attenuated parallel-beam projections. Using transformation of coordinates, this algorithm can be modified to obtain a formulation useful to reconstruct uniformly attenuated fan-beam projections. Unlike that for parallel-beam projections, this formulation does not produce a filtered backprojection reconstruction algorithm but instead has a formulation that is an inverse integral operator with a spatially varying kernel. This algorithm thus requires more computation time than does the filtered backprojection reconstruction algorithm for the uniformly attenuated parallel-beam case. However, the fan-beam reconstructions demonstrate the same image quality as that of parallel-beam reconstructions.**

***Index Terms*—Attenuation correction, fan-beam, image reconstruction.**

I. Introduction

IN DERIVING algorithms to reconstruct single photon emission computed tomography (SPECT) projection data, it is important that the algorithm compensates for photon attenuation in order to obtain quantitative reconstruction results. This is easily done in theory using iterative reconstruction algorithms which attempt to invert the system of linear equations that model the attenuated projections. However, analytical algorithms that correct for photon attenuation are not easily derived, as is evidenced by the fact that to date no analytical filtered backprojection reconstruction algorithm has ever been derived that is capable of obtaining attenuation-corrected reconstructions from constant attenuated fan-beam projections. In this paper, an algorithm is derived for uniformly attenuated fan-beam projections; the equation is not a filtered backprojection algorithm, but an inversion formula characterized for each reconstruction point as a double integral over the projection angle sampling and detector sampling.

Various analytical algorithms for reconstruction of uniformly attenuated projections have been proposed. Bellini *et al*. [2] developed an inverse relationship between the source distribution and the Fourier transform of the projections. Tretiak and Metz [3] developed a filtered backprojection algorithm that specified a method for constructing desired filter functions in the frequency domain. Gullberg and Budinger [4] advanced the theory further by deriving spatial domain convolvers. A number of convolvers corresponding to a variety of apodizing functions were specified. Kim *et al.* [5] gave an exact inversion formula. They proposed a simplification in deriving the inversion formula based on Radon's inverse transform [6]. Hawkins *et al.* [7] derived a circular harmonic transform solution. All of these algorithms were derived for attenuated parallel-beam projections.

In this paper we extend the algorithm derived by Tretiak and Metz for parallel-beam geometry to fan-beam geometry. The implementation of the Tretiak and Metz algorithm for parallel-beam geometry involves a preprocessing step to obtain modified attenuated Radon projections, called exponential Radon projections. To these projections, an attenuation-dependent filter is applied and the result is backprojected via an exponentially weighted backprojector. We start with the filtered backprojection algorithm for the exponential Radon transform and derive a reconstruction formula for exponential attenuated fan-beam projections by transforming coordinates from parallel-beam geometry to fan-beam geometry. This derivation is straightforward, but the reconstruction formula does not produce a convolution backprojection algorithm. The kernel in the inverse integral operator is not only a function of the attenuation coefficient but is also a function of the spatial position of the point to be reconstructed. A double integration is therefore required for every point in the reconstruction.

II. Theory

A. The Derivation of Tretiak and Metz's Algorithm

The coordinate system for the parallel-beam geometry is illustrated in Fig. 1. A two-dimensional (2-D) distribution is represented by a function $f(x,y)$ in the Cartesian coordinate system $O-xy$. The coordinate system $O-st$ is obtained from the coordinate system $O-xy$ by rotating clockwise $\pi/2-\theta$ radians around the origin O. A vector $\vec{x}$ in the $O-xy$ coordinate system is expressed as $\vec{x}=x\vec{i}+y\vec{j}$, where $x=\vec{x}\cdot\vec{i}$ and $y=\vec{x}\cdot\vec{j}$. A vector $\vec{x}$ in the $O-st$ coordinate system is expressed as $\vec{x}=s\vec{\alpha}+t\vec{\theta}$, where $s=\vec{x}\cdot\vec{\alpha}$ and $t=\vec{x}\cdot\vec{\theta}$. The attenuated projections $p_\theta(t)$ of the function $f(x,y)$ are the line integral of $f(x,y)$ with an exponential weighting factor [1]. For constant attenuation coefficient μ, $p_\theta(t)$ is expressed as

$$p_\theta(t)=\int_{-\infty}^{\infty} f(s\vec{\alpha}+t\vec{\theta})e^{-\mu[D_\theta(t)-s]}ds \qquad (1)$$

Manuscript received December 6, 1995; revised January 7, 1997. This work was supported in part by the NIH under Grant RO1 HL39792 and Picker International.

The authors are with the Department of Radiology, University of Utah, Salt Lake City, UT 84132 USA.

Publisher Item Identifier S 0018-9499(97)02791-3.

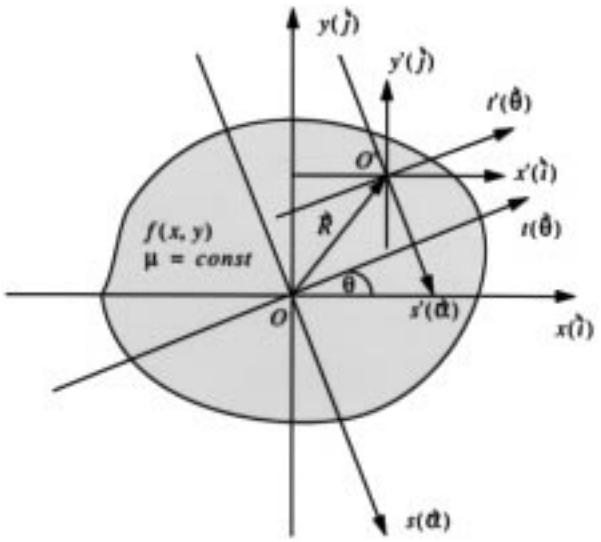

Fig. 1. The 2-D parallel-beam geometry.

where $f(s\vec{\alpha}+t\vec{\theta})$ is the source distribution and $D_\theta(t)$ is the distance from the attenuator edge to the t axis.

If the attenuator is a convex set and the linear attenuation coefficient μ is constant, the exponential Radon transformed projections $q_\theta(t)$ are

$$q_\theta(t)=p_\theta(t)e^{\mu D_\theta(t)}=\int_{-\infty}^{\infty}f(s\vec{\alpha}+t\vec{\theta})e^{\mu s}ds. \tag{2}$$

Notice that the exponential Radon projections $q_\theta(t)$ are formed from the attenuated Radon projections $p_\theta(t)$ by factoring out the attenuation effect from the t axis (through the center of rotation) to the edge of the attenuator.

A fixed point O' inside the attenuator is expressed by a vector $\vec{R}=R_x\vec{i}+R_y\vec{j}$ in the $O-xy$ coordinate system. A new coordinate system $O'-s't'$ is obtained by shifting the coordinate system $O-st$ from O to O'. The point O' can also be expressed by $\vec{R}=R_s\vec{\alpha}+R_t\vec{\theta}$ in the $O-st$ coordinate system. The relationships between the coordinate systems $O-st$ and $O'-s't'$ are

$$s'=s-R_s \tag{3}$$
$$t'=t-R_t \tag{4}$$
$$p'_\theta(t')=p_\theta(t) \tag{5}$$
$$D'_\theta(t')=D_\theta(t)-R_s. \tag{6}$$

In the $O'-s't'$ coordinate system, the exponential Radon transformed projections $q'_\theta(t')$ are

$$\begin{aligned}q'_\theta(t')&=p'_\theta(t')e^{\mu D'_\theta(t')}\\&=\int_{-\infty}^{\infty}f_{(R_x,R_y)}(s'\vec{\alpha}+t'\vec{\theta})e^{\mu s'}ds'\end{aligned} \tag{7}$$

where $f_{(R_x,R_y)}(s'\vec{\alpha}+t'\vec{\theta})$ is the source distribution function in the coordinate system $O'-s't'$. Multiplying both sides by $d\theta$ and integrating from 0 to 2π yields

$$\begin{aligned}\bar{q}'(t')&=\int_0^{2\pi}q'_\theta(t')d\theta\\&=\int_0^{2\pi}\int_{-\infty}^{\infty}f_{(R_x,R_y)}(s'\vec{\alpha}+t'\vec{\theta})e^{\mu s'}ds'd\theta.\end{aligned} \tag{8}$$

Changing the order of integration yields

$$\bar{q}'(t')=\int_{-\infty}^{\infty}\left(\int_0^{2\pi}f_{(R_x,R_y)}(s'\vec{\alpha}+t'\vec{\theta})d\theta\right)e^{\mu s'}ds'. \tag{9}$$

Let

$$\overline{f_{(R_x,R_y)}}(r)=\int_0^{2\pi}f_{(R_x,R_y)}(s'\vec{\alpha}+t'\vec{\theta})d\theta \tag{10}$$

then $\overline{f_{(R_x,R_y)}}(r)$ is the integral of the object distribution function $f(\vec{x})$ on a circle of radius $r=\sqrt{t'^2+s'^2}$ centered at (R_x,R_y). Then (9) can be expressed as

$$\bar{q}'(t')=\int_{-\infty}^{\infty}\overline{f_{(R_x,R_y)}}(r)e^{\mu s'}ds'. \tag{11}$$

Because $\overline{f_{(R_x,R_y)}}(r)$ is an even function, (11) can be rewritten as

$$\bar{q}'(t')=2\int_0^{\infty}\overline{f_{(R_x,R_y)}}(r)\cos\ h(\mu s')ds'. \tag{12}$$

By changing the variable of integration and by using $r=\sqrt{t'^2+s'^2},\ s'=\sqrt{r^2-t'^2},\ ds'=(rdr)/(\sqrt{r^2-t'^2})$, (12) becomes

$$\bar{q}'(t')=2\int_{|t'|}^{\infty}\overline{f_{(R_x,R_y)}}(r)\cos\ h(\mu\sqrt{r^2-t'^2})\frac{rdr}{\sqrt{r^2-t'^2}}. \tag{13}$$

The function $\bar{q}'(t')$ in (13) is the attenuated Abel transform of $\overline{f_{(R_x,R_y)}}(r)$. The inverse attenuated Abel transform is given by [8]

$$\overline{f_{(R_x,R_y)}}(r)=\frac{-1}{\pi}\int_r^{\infty}\frac{d}{dt'}[\bar{q}'(t')]\frac{\cos(\mu\sqrt{t'^2-r^2})}{\sqrt{t'^2-r^2}}dt'. \tag{14}$$

Substituting $-t'$ for t' yields

$$\overline{f_{(R_x,R_y)}}(r)=\frac{1}{\pi}\int_{-\infty}^{-r}\frac{d}{dt'}[\bar{q}'(t')]\frac{\cos(\mu\sqrt{t'^2-r^2})}{\sqrt{t'^2-r^2}}dt'. \tag{15}$$

Averaging (14) and (15) produces the following result:

$$\begin{aligned}\overline{f_{(R_x,R_y)}}(r)=\frac{-1}{2\pi}\Bigg[&\int_r^{\infty}\frac{d}{dt'}[\bar{q}'(t')]\frac{\cos(\mu\sqrt{t'^2-r^2})}{\sqrt{t'^2-r^2}}dt'\\&-\int_{-\infty}^{-r}\frac{d}{dt'}[\bar{q}'(t')]\frac{\cos(\mu\sqrt{t'^2-r^2})}{\sqrt{t'^2-r^2}}dt'\Bigg].\end{aligned} \tag{16}$$

The general solution $f(R_x, R_y)$ is constructed from $\overline{f_{(R_x,R_y)}}(r)$ by using

$$f(R_x, R_y) = \lim_{r\to 0} \frac{1}{2\pi}\left(\overline{f_{(R_x,R_y)}}(r)\right). \tag{17}$$

Evaluating the limit yields the following expression:

$$f(R_x, R_y) = \frac{-1}{4\pi^2}\mathcal{P}\int_{-\infty}^{\infty} \frac{\cos(\mu t')}{t'}\frac{d}{dt'}[\overline{q}'(t')]dt' \tag{18}$$

where $\mathcal{P}\int_{-\infty}^{\infty}$ is the Cauchy principal value integral. Calculating the integral in (18) by parts eliminates the derivative

$$f(R_x, R_y) = \frac{-1}{4\pi^2}\mathcal{P}\int_{-\infty}^{\infty} \frac{\mu t'\sin(\mu t') + \cos(\mu t')}{t'^2}\overline{q}'(t')dt'. \tag{19}$$

Letting

$$h_\mu(t') = -\frac{\mu t'\sin(\mu t') + \cos(\mu t')}{t'^2} \tag{20}$$

and using (5)–(8), (20) can be rewritten as

$$f(R_x, R_y) = \frac{1}{4\pi^2}\mathcal{P}\int_{-\infty}^{\infty} h_\mu(t')\left[\int_0^{2\pi} p_\theta(t)e^{\mu D_\theta(t)-\mu R_s}d\theta\right]dt'. \tag{21}$$

Substituting (4) and (2) into (21), using the fact that $h_\mu(t')$ is an even function, and changing the order of integration, we obtain

$$f(R_x, R_y) = \frac{1}{4\pi^2}\int_0^{2\pi} e^{-\mu R_s}\left[\mathcal{P}\int_{-\infty}^{\infty} h_\mu(R_t - t)q_\theta(t)dt\right]d\theta. \tag{22}$$

Equation (22) is the closed-form inversion formula for the exponential Radon transform.

To implement the formula in (22) by filtering in the frequency domain, the Fourier transform of the convolver $h_\mu(t)$ must be calculated. The Fourier transform is a linear transform, hence the Fourier transform of $h_\mu(t)$ is the sum of the Fourier transform of $(-\mu\sin[\mu t])/t$ and the Fourier transform of $(-\cos[\mu t])/t^2$. The Fourier transform of $(-\mu\sin[\mu t])/t$ is [9]

$$\mathcal{F}\left\{-\frac{\mu\sin[\mu t]}{t}\right\} = -\pi\mu\prod\left(\frac{\pi\nu}{\mu}\right) \tag{23}$$

where $\mathcal{F}$ is the Fourier transform operator and $\Pi(x)$ is the rectangle function. The Fourier transform of $(-\cos[\mu r])/r^2$ is

$$\mathcal{F}\left\{-\frac{\cos[\mu t]}{t^2}\right\} = 2\pi^2|\nu|H\left(|\nu| - \frac{\mu}{2\pi}\right) + \pi\mu\prod\left(\frac{\pi\nu}{\mu}\right) \tag{24}$$

where $H(x)$ is the Heaviside unit step function. By adding (23) and (24), the Fourier transform of $h_\mu(r)$ is given by

$$\mathcal{F}\{h_\mu(r)\} = 2\pi^2|\nu|H\left(|\nu| - \frac{\mu}{2\pi}\right). \tag{25}$$

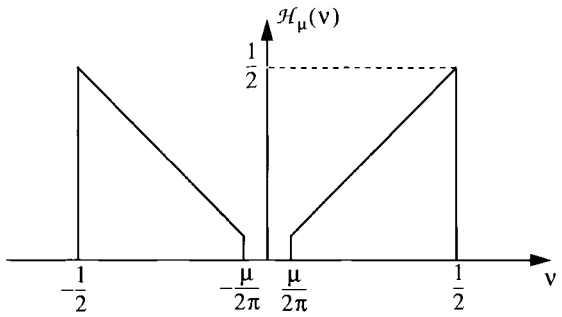

Fig. 2. The notch filter.

Using the result in (25) and changing (22) from convolution to filtering produces the following expression for the implementation of (22) in the frequency domain:

$$f(R_x, R_y) = \frac{1}{2}\int_0^{2\pi} e^{-\mu R_s} \times\left[\mathcal{F}^{-1}\left(|\nu|H\left(|\nu| - \frac{\mu}{2\pi}\right)\mathcal{F}(q_\theta(t))\right)\right]d\theta. \tag{26}$$

Projection data are sampled with a sampling interval of one pixel. If there is no aliasing, which implies that the projections contain zero energy outside the frequency interval $(-1/2, 1/2)$ cycles/pixel, the filter in the frequency domain can be apodized as shown in Fig. 2. This is called the notch filter $\mathcal{H}_\mu(\nu)$, which has the expression

$$\mathcal{H}_\mu(\nu) = \begin{cases} |\nu|H(|\nu| - \mu/(2\pi)), & |\nu| < 1/2 \\ 0, & |\nu| \geq 1/2. \end{cases} \tag{27}$$

An approximate implementation of (22) is to perform a convolution in the spatial domain

$$f(R_x, R_y) = \frac{1}{2}\int_0^{2\pi} e^{-\mu R_s}\left(\int_{-\infty}^{\infty}\hat{h}_\mu(R_t - t)q_\theta(t)dt\right)d\theta \tag{28}$$

where the convolver $\hat{h}_\mu(t)$ is obtained by calculating the inverse Fourier transform of $\mathcal{H}_\mu(\nu)$ to obtain

$$\hat{h}_\mu(t) = \mathcal{F}^{-1}[\mathcal{H}_\mu(\nu)] = 2\int_{\mu/(2\pi)}^{1/2}\nu\cos(2\pi\nu t)dt = \left(\frac{\pi\sin(\pi t) - \mu\sin(\mu t)}{2\pi^2 t} + \frac{\cos(\pi t) - \cos(\mu t)}{2\pi^2 t^2}\right). \tag{29}$$

This is the convolution backprojection algorithm for the exponential Radon transform with convolver $\hat{h}_\mu(t)$. For t equal to an integer number n, the convolver becomes

$$\hat{h}_\mu(n) = \begin{cases} \frac{1}{4} - \frac{\mu^2}{4\pi^2}, & n = 0 \\ \frac{-\mu\sin(\mu n)}{2\pi^2 n} + \frac{1-\cos(\mu n)}{2\pi^2 n^2}, & n = \text{even} \\ \frac{-\mu\sin(\mu n)}{2\pi^2 n} - \frac{1+\cos(\mu n)}{2\pi^2 n^2}, & n = \text{odd}. \end{cases} \tag{30}$$

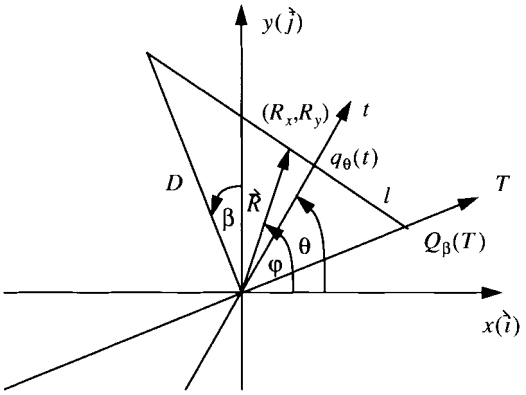

Fig. 3. The 2-D fan-beam geometry.

Here the filtered backprojection algorithm for the exponential Radon transform was derived based on the work of Radon [6] and Kim *et al.* [5]. The filter function in (29) is the same as that derived by Gullberg and Budinger [4].

B. The Extension of Tretiak and Metz's Algorithm to Fan-Beam Geometry

The 2-D fan-beam geometry is illustrated in Fig. 3. The exponential fan-beam projections $Q_\beta(T)$ and the corresponding exponential Radon (parallel-beam) projections $q_\theta(t)$ for the line l are equal if

$$t = (TD)/(D^2+T^2)^{1/2} \tag{31}$$

and

$$\theta = \beta + \tan^{-1}\frac{T}{D} \tag{32}$$

where D is the fan-beam focal length.

The algorithm developed in the previous section for parallel-beam geometry can be extended to fan-beam geometry by using the coordinate system transformation expressed in (31) and (32). The Jacobian $|J|$ of the transformation (i.e., $dtd\theta = |J|dTd\beta$) is

$$|J| = \left|\begin{matrix}\frac{\partial\theta}{\partial T} & \frac{\partial t}{\partial T}\\ \frac{\partial\theta}{\partial\beta} & \frac{\partial t}{\partial\beta}\end{matrix}\right| = \left|\begin{matrix}\frac{D}{D^2+T^2} & \frac{D^3}{(D^2+T^2)^{3/2}}\\ 1 & 0\end{matrix}\right| = \frac{D^3}{(D^2+T^2)^{3/2}}. \tag{33}$$

Transforming coordinates and using the expression for the Jacobian in (33), the convolution backprojection algorithm for the exponential Radon (parallel-beam) transform in (28) can be written for fan-beam geometry as

$$f(R_x,R_y) = \frac{1}{2}\int_0^{2\pi} e^{-\mu\hat{R}_s} \times\left(\int_{-\infty}^{\infty}\hat{h}_\mu\left(R_t - \frac{TD}{\sqrt{D^2+T^2}}\right)Q_\beta(T)|J|dT\right)d\beta \tag{34}$$

where

$$\hat{R}_s = R_x\sin\left(\beta+\tan^{-1}\frac{\hat{T}}{D}\right) - R_y\cos\left(\beta+\tan^{-1}\frac{\hat{T}}{D}\right) \tag{35}$$

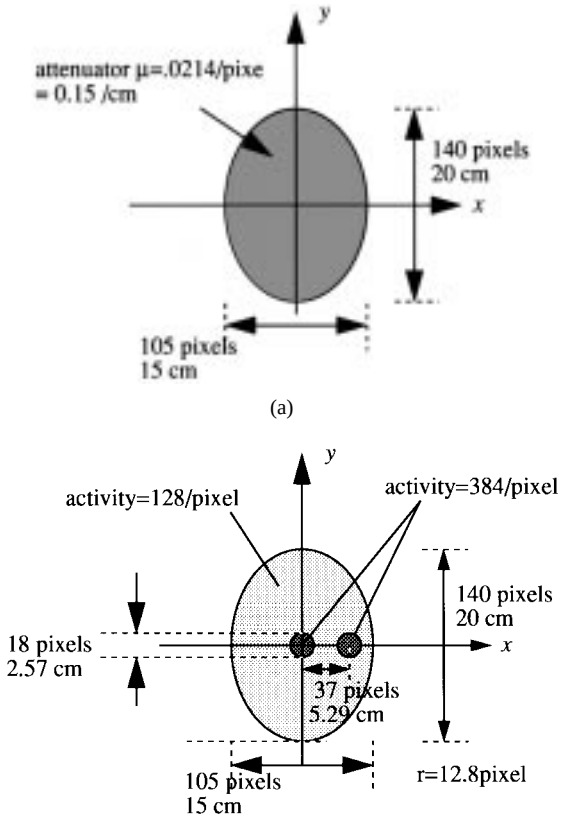

Fig. 4. Phantom used in computer simulations: (a) attenuator and (b) source activity.

and

$$R_t = R_x\cos\left(\beta+\tan^{-1}\frac{T}{D}\right) + R_y\sin\left(\beta+\tan^{-1}\frac{T}{D}\right). \tag{36}$$

The symbol $\hat{T}$ differs from the variable T in that it is a fixed location where the reconstruction point (R_x, R_y) projects onto the detector.

Equation (34) is the analytical inverse formula for exponential fan-beam projections. Compared with (28), the filter function for fan-beam geometry is not a convolver. For each point (R_x, R_y), the reconstruction has to be evaluated by numerically calculating the double integral in (34). This is not as computationally efficient as the convolution implementation for parallel-beam geometry in (28).

III. Methods

Tretiak and Metz's algorithm for the parallel-beam geometry and its extension to the fan-beam geometry was implemented in C on a SUN ULTRAServer 170 (one 167-MHz UltraSPARC processor). This was compared with the iterative expectation maximization-maximum likelihood (EM-ML) reconstruction algorithm in computer simulations for both parallel-beam and fan-beam geometries.

The phantom used in the simulation is shown in Fig. 4. This 2-D phantom consists of two small circular discs and one large elliptical disc. The activity in the large elliptical

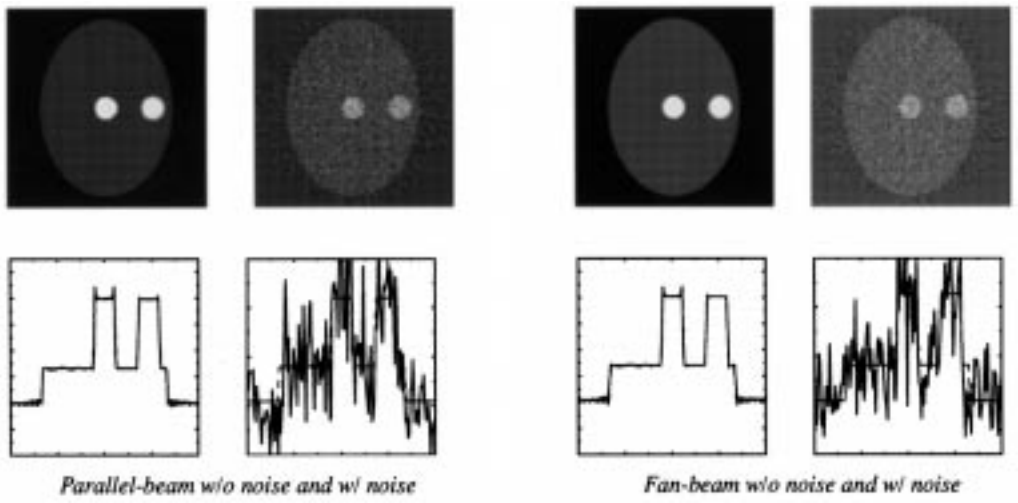

Fig. 5. Images reconstructed from nonattenuated projections.

disc was 128 counts per pixel, and the small discs were 384 counts per pixel. The 15 × 20-cm attenuator had an attenuation coefficient of 0.15 cm^{-1}. This corresponded to a pixel size of 0.143 cm with an attenuation coefficient of 0.0214 per pixel. All reconstructions were 157 × 157.

In the computer simulations, the attenuated projections were generated analytically by evaluating the line integrals with an exponential attenuation weighting function. Both parallel-beam and fan-beam projections had 157 detection bins and 512 views uniformly sampled over 360°. The orbit of the focal point was a circle with a focal length of 350 pixels (50 cm). For the studies with noise, Poisson noise was added to the projection data, which had a total of 579 190 counts for the parallel-beam and 587 012 counts for the fan-beam geometry.

The algorithm for reconstructing exponential fan-beam projections was implemented using the following steps.

I. The simulated projections were first multiplied by an exponential weighting factor $e^{\mu D_\theta(T)}$, similar to what was done for parallel-beam geometry in (2) to obtain the fan-beam exponential projections $Q_\beta(T)$.

II. For each point (R_x, R_y) the double integral in (34) was evaluated.

A. For a fixed β:

1) the fan-beam exponential projections $Q_\beta(T)$ were weighted by the Jacobian $|J|$;
2) the inner integral in (34) was evaluated by summing the integrand over discrete values of T. At each discrete value:
   a) R_t was evaluated;
   b) $\hat{h}_\mu(t)$ was evaluated;
   c) The terms in a) and b) were multiplied with the weighted exponential projections $Q_\beta(T)|J|$;
   d) the results in c) were summed over the discrete values of T.
3) backprojection:
   a) $\hat{R}_s$ was evaluated;
   b) $e^{-\mu\hat{R}_s}$ was evaluated;
   c) $e^{-\mu\hat{R}_s}$ was multiplied by the result from 2)-d) and backprojected.

B. The image at (R_x, R_y) was obtained by summing the result in 3)-c) over all projection angles β.

III. The image was obtained by performing the double integral for each point (R_x, R_y).

The parallel-beam and fan-beam implementations differ. For the parallel-beam geometry, the reconstruction is obtained by filtering independent of the reconstruction coordinate followed by a backprojection, whereas for the fan-beam geometry the filter depends on the reconstruction coordinate.

IV. Results

The reconstructions of parallel-beam and fan-beam geometries are shown in Figs. 5–8. All profiles are drawn at the middle of the image horizontally. The dotted profile is the ideal profile with which to be compared. Each image is scaled and displayed according to its own maximum and minimum values.

Fig. 5 shows the images reconstructed from unattenuated projection data using the conventional filtered backprojection algorithm for both parallel-beam and fan-beam geometries. Here both parallel-beam and fan-beam algorithms give accurate reconstructions, and they are not sensitive to noise. The reconstruction time for the parallel-beam and fan-beam geometries was approximately 30 s. The images in Fig. 5 were used as a standard to compare with.

Fig. 6 shows the images reconstructed from attenuated projection data using the filtered backprojection algorithm. Notice that for the attenuated projections, severe artifacts of reduced intensity are observed in the center of the image if the reconstruction algorithms do not compensate for the attenuation. The reconstruction time for the parallel-beam fan-beam geometries was approximately 30 s.

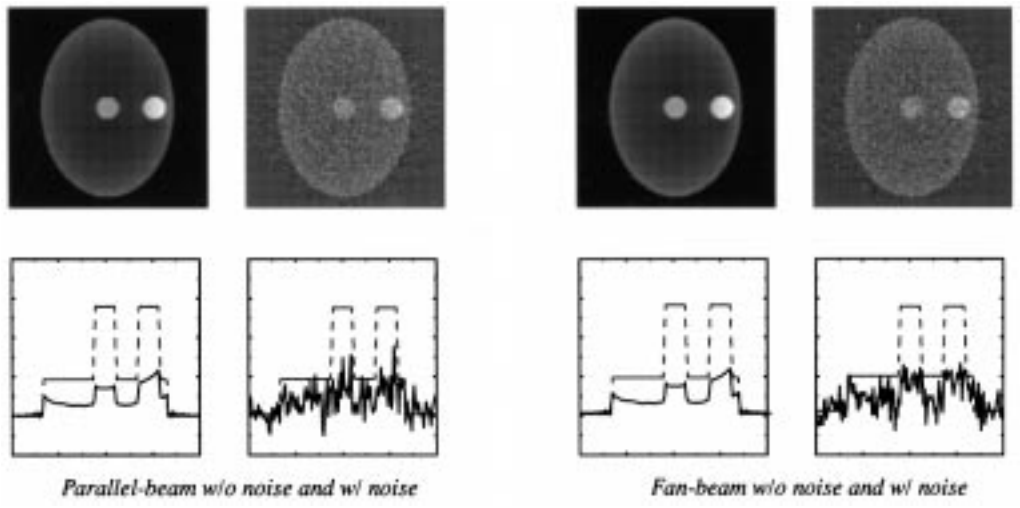

Fig. 6. Images reconstructed from attenuated projections without attenuation correction.

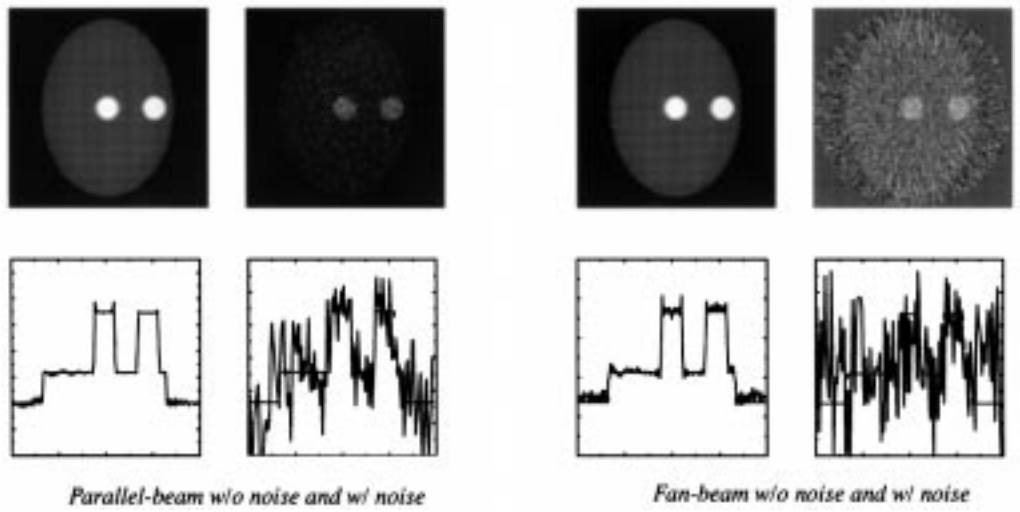

Fig. 7. Images reconstructed from attenuated projections with attenuation correction.

Fig. 7 shows the images reconstructed from the same projection data as in Fig. 6 but using the attenuation correction algorithm developed in this paper. The newly developed algorithm is capable of compensating for constant attenuation, but both parallel-beam and fan-beam reconstructions have radial streak artifacts caused by angular aliasing and noise. The amplification of the artifacts is due to the exponential weighting function in the backprojector and is dependent upon the source distribution. The reconstruction time for the parallel-beam geometry was approximately 30 s and for the fan-beam geometry was approximately 10 000 s.

Fig. 8 shows the results of EM-ML reconstructions after 40 iterations. The reconstruction times for the parallel and fan-beam geometries was approximately 700 s.

V. Discussion

An integral inverse formulation with a spatially varying kernel has been developed to reconstruct uniformly-attenuated fan-beam projections. Unlike the algorithm for attenuated parallel-beam projections, this formulation cannot be implemented as a filtered backprojection algorithm. Therefore, the algorithm for fan-beam geometry requires more computation time (even longer than that for an iterative EM-ML reconstruction algorithm), but the simulations show results equivalent to that for parallel-beam reconstruction algorithms. In the case of noise the fan-beam algorithm amplifies noise similar to that demonstrated previously for parallel-beam geometry [4].

If a reconstruction algorithm can be formulated as a filtering followed by a backprojection operation, the reconstruction is very efficient. This can be done for parallel-beam geometry with uniform attenuation. However, the analytical approach presented in this paper for the uniformly attenuated fan-beam geometry cannot be formulated as a filtered backprojection algorithm. For that reason its reconstruction times are actually much slower than the 40 iterations of the EM-ML algorithm: 10 000 versus 700 s. An analytical approach is preferred also because a solution is obtained, giving the opportunity

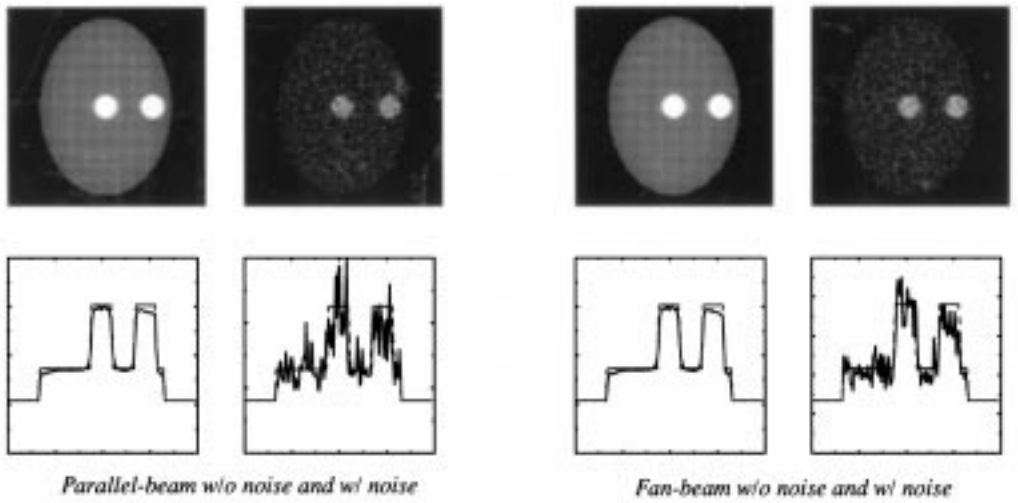

Fig. 8. Iterative ML-EM images reconstructed from attenuated projections with attenuation correction (after 40 iterations).

to better understand the bias and variance of the reconstructed image. This is difficult for an iterative reconstruction algorithm because it has to be analyzed as a function of iteration number.

The simulations were performed with data that simulated SPECT noise levels. The results in the simulations were not filtered. To deal with noise, an apodizing factor that rolled off the "ramp filter" could be used. For the fan-beam application the "ramp filter" is no longer truly a filter (i.e., a spatial convolution) but a kernel of an inverse integral operator. The addition of an apodizing factor also changes the point response of the reconstruction. Another approach would be to perform a three-dimensional post-filtering.

This algorithm does not handle noise very well, even with some kind of apodizing filter. This drawback was also reported for the parallel-beam geometry several years ago [4]. Both fan-beam and parallel-beam reconstructions with noise look much worse than the noise-free reconstruction due to the exponential amplifying factor in the backprojection step. It is worthwhile to investigate a method to suppress the noise amplification in this algorithm.

The attenuation correction fan-beam reconstruction algorithm may have clinical significance for brain SPECT in those cases of high counting statistics. It could be useful to obtain an estimate of the bias and variance of the attenuation corrected reconstruction values.

ACKNOWLEDGMENT

The authors would like to thank the Biodynamics Research Unit of the Mayo Foundation for use of the Analyze software package.

REFERENCES

[1] G. T. Gullberg, "The attenuated Radon transform: Theory and application in medicine and biology," Ph.D. dissertation, Univ. California, Berkeley, 1979.
[2] S. Bellini, M. Piacentini, C. Cafforio, and F. Rocca, "Compensation of tissue absorption in emission tomography," *IEEE Trans. Acoust. Speech Signal Processing,* vol. 27, pp. 213–218, 1979.
[3] O. Tretiak and C. Metz, "The exponential Radon transform," *SIAM J. Appl. Math.*, vol. 39, pp. 341–354, 1980.
[4] G. T. Gullberg and T. F. Budinger, "The use of filtering methods to compensate for constant attenuation in single-photon emission computed tomography," *IEEE Trans. Biomed. Eng.*, vol. 28, pp. 142–157, 1981.
[5] R. I. Kim, R. P. Tewarson, Y. Bizais, and R. W. Rowe, "Inversion for the attenuated Radon transform with constant attenuation," *IEEE Trans. Nucl. Sci.*, vol. 31, pp. 538–542, 1984.
[6] J. Radon, "Uber die Bestimmung von Funktionen durch ihre Integralwerte Langs gewisser Mannigfaltigkeiten," *Berichte Sachsische Akademie der Wissenschaften. Leipzig, Math. Phys.*, Kl. vol. 69, pp. 262–279, 1917.
[7] W. G. Hawkins, P. K. Leichner, and N. C. Yang, "The circular harmonic transform for SPECT reconstruction and boundary conditions on the Fourier transform of the sinogram," *IEEE Trans. Med. Imaging*, vol. 7, pp. 135–148, 1988.
[8] A. V. Clough and H. Barrett, "Attenuated Radon and Abel transform," *J. Opt. Soc. Am.*, vol. 73, pp. 1590–1595, 1983.
[9] R. N. Bracewell, *The Fourier Transform and Its Applications*, 2nd ed. New York: McGraw-Hill, 1986, p. 123.